



Original Articles

scRNA-seq of colorectal cancer shows regional immune atlas with the function of CD20⁺ B cells

Linlin Ji ^{a,1}, Gongbo Fu ^{a,b,c,d,*1}, Mengxi Huang ^{a,1}, Xiaoming Kao ^{e,1}, Jialong Zhu ^{b,1}, Zhe Dai ^a, Yitian Chen ^a, Huiyu Li ^a, Jie Zhou ^{f,**}, Xiaoyuan Chu ^{a,b,c,d,***}, Zengjie Lei ^{a,b,c,d,****}

^a Department of Medical Oncology, Nanjing Jinling Hospital, Affiliated Hospital of Medical School, Nanjing University, Nanjing, 210000, China

^b Department of Medical Oncology, Jinling Hospital, The First School of Clinical Medicine, Southern Medical University, Nanjing, 210000, China

^c Department of Medical Oncology, Jinling Hospital, Nanjing Medical University, Nanjing, 210000, China

^d Department of Medical Oncology, Jinling Hospital, Nanjing University of Chinese Medicine, Nanjing, 210000, China

^e Department of General Surgery, Jinling Hospital, Nanjing Medical University, Nanjing, 210000, China

^f Department of Oncology and Southwest Cancer Center, Southwest Hospital, Army Medical University (Third Military Medical University), Chongqing, 400038, China

ARTICLE INFO

Keywords:
scRNA-seq
Colorectal cancer
Regional immune atlas
B cells
Immunotherapy

ABSTRACT

Colorectal cancer (CRC) from different regions exhibits different histological, genetic characteristics, and molecular subtypes, even in response to conventional chemotherapies and immunotherapies. To characterize the immune landscape in different regions of CRC and search for potential therapeutic targets, we analyzed 39,484 single-cell transcription data from 19 samples of CRC and paired normal tissues from four regions to identify the immune characteristics of CRC among anatomic locations, especially in B cells. We discovered that immune cell infiltration in tumors significantly varied among different regions of CRC. B cells from right- and left-sided CRC had different development trajectories, but both had extensive interactions with myeloid cells and T cells. Survival analysis suggested that CD20⁺ B cells correlated with good prognosis in CRC patients, especially on the right side. Furthermore, the depletion of CD20⁺ B cells demonstrated that anti-CD20 promoted tumor growth progression and reversed the tumor-killing activity of anti-PD-1 treatment *in vivo* and *in vitro*. Our results highlight the characterization of the immune landscape of CRC in different regions. CD20⁺ B-cell infiltration has been associated with CRC patient prognosis and may promote the tumor-killing role of PD-1 antibodies.

1. Introduction

According to the most recent Global Cancer Statistics 2020 [1], colorectal cancer (CRC) is the third most common cancer globally and ranks second in lung cancer mortality. Radical resection remains the cornerstone for treating CRC patients with stage I/II [2]. However, most CRC patients are diagnosed at a more advanced stage (III/IV), often due to the absence of significant early symptoms or socioeconomic factors, particularly in developing and less developed countries. For patients with stage III/IV CRC, treatments such as radiotherapy, adjuvant

chemoradiotherapy, and targeted therapy are available; however, their efficacy remains limited due to insensitivity and drug resistance [3]. Immunotherapy has become a clinical reality, with ongoing preclinical and clinical studies demonstrating that an existing intratumor adaptive immune response is essential for the effectiveness of such therapies. Consequently, it is imperative to thoroughly investigate the tumor microenvironment (TME) of CRC, with a particular focus on the immune microenvironment.

Tumors located on the right and left sides exhibit distinct histological, genetic, and molecular characteristics, which translate into varying

* Corresponding author. Department of Medical Oncology, Nanjing Jinling Hospital, Affiliated Hospital of Medical School, Nanjing University, Nanjing, 210000, China.

** Corresponding author.

*** Corresponding author. Department of Medical Oncology, Jinling Hospital, The First School of Clinical Medicine, Southern Medical University, Nanjing, 210000, China.

**** Corresponding author. Department of Medical Oncology, Nanjing Jinling Hospital, 305 Zhongshan East Road, Xuanwu District, Jiangsu Province, China.

E-mail addresses: mhksf@126.com (G. Fu), zhoujie_fl@163.com (J. Zhou), chuxiaoyuan000@163.com (X. Chu), leizengjie@163.com (Z. Lei).

¹ These authors contributed equally to this work.

responses of CRC to conventional chemotherapies and immunotherapies [4,5]. The discrepancy in CRC location can be partly attributed to embryological origins, with the right-sided colon derived from the midgut and the left-sided from the hindgut. Furthermore, the frequencies of mutations in various oncogenes and tumor suppressor genes differed between the left and right sides. BRAF mutations, which are more prevalent in right-sided CRC, are associated with poorer prognosis in advanced stages of the disease, whereas APC and TP53 mutations occur more frequently in left-sided CRC [6,7]. In addition, tyrosine kinase receptors such as ERBB2 and EGFR are more frequently upregulated in left-sided cancers, elucidating the ineffectiveness of anti-EGFR-targeted drugs in right-sided tumors [2,4]. Conversely, markers such as CpG island methylation and microsatellite instability, which correlate with immunotherapy efficacy, exhibit higher levels in right-sided cancers and may confer a better prognosis in stage II tumors of the right side [6,7]. In summary, CRCs originating from different anatomical locations exhibit genetic and molecular disparities that could influence immunotherapy efficacy and overall prognosis.

The emergence of single-cell sequencing technology has significantly advanced our understanding of TME in tumors. Consequently, the complexity of tumor contexture and the diversity of cellular populations have been extensively elucidated. Phenotypic states fulfill multiple roles in tumor initiation and progression [8,9]. The prevailing model of TME posits an environment of immune tolerance within tumors [10]. CD8⁺ T-cells in tumors exhibit an exhausted phenotype, whereas CD4⁺ Treg cells, which accumulate in tumors, inhibit immune cytotoxic activity [11,12]. Additionally, other immune cells, including MDSC [13] and M2-like macrophages [14], contribute to immune tolerance. Zhang et al. demonstrated that tumor-infiltrating myeloid cells in CRC constitute a complex population with diverse cell types exerting varied influences on CRC [15]. Lee HO et al. utilized extensive parallel single-cell RNA sequencing data to uncover the diversity of cellular components that define the molecular subtypes of CRC and their dynamic interplay [16]. Guo et al. offered a preliminary characterization of the disparities between left- and right-sided CRC using single-cell transcriptome data [17]. Recently, research on the role and therapeutic potential of tumor-infiltrating B cells in solid tumors has expanded with the advent of single-cell sequencing technology. Three research teams have identified that B cells with tertiary lymphoid structures (TLSs) can serve as predictors of immunotherapy efficacy [18–20]. CHEN et al. reported that CD20⁺ tumor-infiltrating B cells in lung cancer can inhibit the growth of NSCLC by secreting high levels of VNN2 and SERPINA9 and through immunoglobulin endocytosis facilitated by AP2 complexes [21]. Another study clarified the impact of B cells and TLS on immunotherapy in breast cancer, both at the single-cell level and clinically, by analyzing single-cell sequencing data from breast cancer samples and identifying CD23 as a marker for TLS [22]. Furthermore, WANG et al. [23] suggested that IgA⁺IGLC2⁺ plasma cells are correlated with a favorable prognosis in CRC. Given that this field remains nascent, the role of B cells in CRC warrants further exploration.

Here, we constructed a comprehensive profile of CRC immune compartments from different locations, examined their immune contexture heterogeneity, and confirmed the potential role of tumor-infiltrating CD20⁺ B cells. Our findings demonstrate that CRC exhibits significant regional characteristics, and infiltrating CD20⁺ B-cells are associated with the benefit of immune checkpoint blockage.

2. Materials and methods

2.1. Sample collection and processing

Human CRC specimens and patient clinical data were collected from Jinling Hospital following approval by the Jinling Hospital Research Ethics Committee. All diagnoses were validated by pathological analysis. Informed consent was secured under the supervision of a board-certified pathologist. Human tissue specimens were obtained during

surgical resection of tumor samples. Two adjacent normal tissues, two tumor tissues, and one paired liver metastasis sample were acquired from each of the two patients for scRNA-seq (data stored in Gene Expression Omnibus (GEO) at GSE221575).

2.2. Tissue dissociation and preparation

Freshly obtained tissues were placed in the sCellLiveTM Tissue Preservation Solution (Singleron) and kept on ice for 30 min post-surgery. The specimens were rinsed thrice with Hanks Balanced Salt Solution (HBSS), chopped into small pieces, and subsequently digested with 3 mL sCellLiveTM Tissue Dissociation Solution (Singleron) using the Singleron PythoN™ Tissue Dissociation System for 15 min at 37 °C. The cell suspension was harvested and passed through a 40 µm sterile strainer. Following the addition of the GEXSCOPE® red blood cell lysis buffer (RCLB, Singleron), the mixture [Cell: RCLB = 1:2 (volume ratio)] was incubated at room temperature for 5–8 min to lyse red blood cells. Subsequently, the mixture was centrifuged at 300×g at 4 °C for 5 min to discard the supernatant and gently resuspended in phosphate-buffered saline (PBS). Finally, the samples were treated with Trypan Blue, and cell viability was assessed under a microscope.

2.3. Reverse transcription (RT), amplification, and library construction

Single-cell suspensions at a concentration of 2×10^5 cells/mL in PBS (HyClone) were introduced into a microwell chip using the Singleron Matrix® Single Cell Processing System. Subsequently, barcoding beads were retrieved from the microwell chip, enabling reverse transcription (RT) of the mRNA captured by the beads to synthesize cDNA, followed by polymerase chain reaction (PCR) amplification. The amplified cDNA was then fragmented and combined with sequencing adapters. scRNA-seq libraries were assembled using the GEXSCOPE® Single Cell RNA Library Kits (Singleron) [24]. Individual libraries were diluted to a final concentration of 4 nM, pooled, and sequenced on an Illumina Novaseq 6000 system, generating 150 bp paired-end reads.

2.4. Primary raw read data analysis

Raw reads from scRNA-seq were processed to generate gene expression matrices using the CeleScope v1.9.0 pipeline (<https://github.com/singleron-RD/CeleScope>). Initially, raw reads were refined using CeleScope to discard low-quality reads and Cutadapt v1.17 [25] to eliminate poly-A tail and adapter sequences. Cell barcodes and unique molecular identifiers (UMI) were also extracted. Subsequently, STAR v2.6.1a [26] aligned the reads to the reference genome GRCh38 (Ensembl version 92 annotation). The featureCounts v2.0.1 [27] software was employed to quantify the UMI and gene counts for each cell, culminating in the creation of expression matrix files for further analysis.

2.5. Contamination removal

The expression levels of cell marker genes were displayed using FeaturePlot in the Seurat package v3.1.2. Subsequently, RNA was removed using the decontX algorithm in Celda package v.1.3.8 to address this issue [28]. The decontX algorithm presumed K cell populations and utilized Bayesian variational inference to infer ambient RNA contamination as a weighted combination of cell population distributions. This algorithm required the raw UMI counts and several cell populations, calculated using the FindClusters function in the Seurat package v3.1.2, as input, thereby producing a decontaminated count matrix originating from the raw data. A default random seed was applied for consistent reproducibility throughout the entire analysis.

2.6. Quality control

Sc-RNA data from GSE132465 were retrieved from the Gene Expression Omnibus (GEO) database. Seurat's CCA-based alignment was executed to achieve a batch-corrected space with integration anchors determined by the top 20 principal components from the PCA. 1) Cells with a gene count less than 200 or with a higher gene count than specified were removed; 2) cells with a UMI count exceeding 30,000 were excluded; 3) cells with mitochondrial content greater than 50 % were eliminated; 4) genes expressed in fewer than five cells were discarded. After filtering, the remaining cells were retained for subsequent analyses.

2.7. Dimension reduction and clustering

Functions from Seurat v3.1.2 [29] were used for dimension reduction and clustering. Subsequently, the NormalizeData and ScaleData functions were applied to normalize and scale all gene expressions, and the FindVariableFeatures function was utilized to select the top 2000 variable genes for principal component analysis (PCA). The cells were partitioned into multiple clusters with the top 20 principal components using the FindClusters function. The batch effect between samples was mitigated by Harmony [30]. Finally, the t-distributed stochastic neighbor embedding (tSNE) algorithm was employed to visualize the cells in a two-dimensional space.

2.8. Differentially expressed genes (DEGs) analysis

The FindMarkers function in Seurat was utilized to identify DEGs using the Wilcox likelihood-ratio test with default parameters. Genes expressed in more than 10 % of the cells within a cluster, with an average log (Fold Change) value greater than 0.25, were considered DEGs. To annotate the cell types within each cluster, canonical marker expression in DEGs was combined with relevant information from the literature. The marker expression of each cell type was visualized using heatmaps generated with the Seurat DoHeatmap function. Doublet cells were identified and manually removed based on their expression of markers corresponding to distinct cell types.

2.9. Cell type annotation

The cell type identity of each cluster was determined by identifying canonical marker expression within DEGs using the SynEcoSys database. Feature and violin plots depicting marker expression for each cell type were generated using Seurat v3.1.2 FeaturePlot and Vlnplot. More information on the specific markers utilized to define the various cell types is found in [Supplementary Table 5](#).

2.10. Pathway enrichment analysis

Gene Ontology (GO) and Kyoto Encyclopedia of Genes and Genomes (KEGG) analysis were performed with the “clusterProfiler” R package 3.16.1 [31] to explore the potential functions of DEGs. Pathways with a p adj value less than 0.05 were deemed significantly enriched. GO gene sets, encompassing molecular function (MF), biological process (BP), and cellular component (CC) categories, served as reference datasets. Gene set enrichment analysis (GSEA) was conducted on DEGs using the GSVA package, with the average gene expression of each cell type serving as input data [32].

2.11. Trajectory analysis

The cell differentiation trajectory was reconstructed using Monocle2 [33]. Highly variable genes (HVGs) were identified and used to order cells based on spatiotemporal differentiation. DDRTree was employed for feature selection and dimension reduction using the

FindVariableFeatures function. Subsequently, the plot_cell_trajectory function was applied to visualize the trajectory. Additionally, CytoTRACE [34], a computational method that predicts cell differentiation states based on gene counts and expression from single-cell RNA-sequencing data, was employed to predict the differentiation potential of monocyte subpopulations.

2.12. Cell-cell interaction analysis

Cell-cell interaction analysis was conducted using CellPhoneDB v2.1.0 [35] based on known receptor-ligand interactions between two cell types/subtypes. Cluster labels of all cells were randomly permuted 1000 times to calculate the null distribution of average ligand-receptor expression levels of the interacting clusters. Individual ligand or receptor expression was thresholded with a cutoff value based on the average log gene expression distribution for all genes across all cell types. Significant cell-cell interactions were defined as those with p-value <0.05 and average log expression >0.1 and were visualized using the circlize v0.4.10 R package. Moreover, NicheNet ver. 1.0.0 [36] was used to predict cell-cell interactions between CD20⁺ B cells and other immune cells by combining gene expression data from our sequencing cohort with a database of prior knowledge of signaling and gene regulatory networks. The NicheNet Seurat wrapper ('nicenet_seuratobj_aggregate') was applied to an integrated Seurat object containing adjacent normal and tumor tissues. Receiver cells were defined as immune cells except for CD20⁺ B cells, sender cells as CD20⁺ B cells, and the experimental condition was disease state. Ligands expressed by one or more sender cells were ranked based on the Pearson correlation coefficient between the ligand's target predictions and observed transcriptional response. Receiver cell receptors were inferred using the NicheNet prebuilt prior model, which utilizes several curated ligand-receptor and signaling databases to predict links between sender ligands, receiver receptors, and downstream target genes.

2.13. Immune infiltration analysis

Immune infiltration analysis for GSE44076 and GSE50760 datasets was estimated using the CIBERSORT-ABS algorithm with TIMER2.0 (<http://timer.comp-genomics.org/>) [37]. This algorithm provides estimations of various immune cell types, including B cells, CD4⁺ T cells, CD8⁺ T cells, macrophages, and dendritic cells.

2.14. Immunohistochemical and immunofluorescence staining

CRC tissue microarrays (HColA180Su12, HRec-Ade180Sur-05) were purchased from Shanghai Xinchao Biological Co., Ltd. IHC specimens were obtained from surgically resected tumor samples and were formalin-fixed and paraffin-embedded. Sectioning and immunohistochemical (IHC) staining were performed, and all sections were deparaffinized, rehydrated, and washed. Endogenous peroxidase was blocked with 3 % hydrogen peroxide for 15 min, and antigen retrieval was performed by heating it in a water bath. The slides were then incubated with primary antibodies, followed by horseradish peroxidase (HRP)-linked secondary antibodies and stained with diaminobenzidine. Slides were counterstained with hematoxylin and dehydrated with sequential ethanol washes. Two pathologists who were blinded to clinical data independently assessed CD20 and CD3 staining results, and the positively stained cells were manually quantified. The mean number from each patient sample was obtained, and the cell density (number/mm²) of the cell of interest was calculated using ImageJ based on the area of each tumor field. The p-values and correlation coefficients (r) between CD20 and CD3 densities were calculated using Pearson's correlation test and GraphPad Prism V9.0.0. IHC staining of formalin-fixed, paraffin-embedded mouse CT26 specimens was performed in the same way as for CRC specimens.

For human CRC and CT26 tumor tissue slides, permeabilization with

0.3 % Triton X-100 in PBS was performed for 10 min. The cells were blocked with 5 % bovine albumin (BSA) for 30 min at 37 °C and incubated overnight at 4 °C with anti-CD3 and anti-CD20 antibodies. The slides were then washed with PBS, incubated with the corresponding secondary antibody for 30 min at 37 °C, and nuclear stained with 4',6-diamidino-2-phenylindole (DAPI staining solution) for 5 min. Fluorescence images were acquired using a fluorescence microscope (Olympus, Tokyo, Japan). *Supplementary Table 3* lists more information on the primary antibodies used for immunohistochemical and immunofluorescence staining.

2.15. Survival analysis

The counts data of colon adenocarcinoma (COAD) and rectal adenocarcinoma (READ) were obtained from the Genomic Data Commons (GDC) database and normalized with DEseq2 [38]. The patients were grouped into high- and low-expression groups based on the median value of the signature genes related to B cells. Kaplan–Meier (KM) plots were generated using the survival data of these two groups to analyze their overall survival rates.

For IHC results, Kaplan–Meier univariate survival analysis was performed by classifying patients as ‘low’ or ‘high’ based on the median densities of the cells of interest. The log-rank (Mantel-Cox) test was used to calculate p-values and assess the significance of the differences in survival between the two groups.

2.16. Animal studies

All mouse experiments were approved by the Institutional Animal Care and Use Committee of Jinling Hospital. Balb/c mice, aged 6–8 weeks, were obtained from Zihe Biotechnology Co., Ltd in Taizhou, Jiangsu Province. The CT26 mouse colon cancer cell line was purchased from Shanghai Zhongqiao Xinzhou Biotechnology Co., Ltd.

In the experiment, Balb/c mice were subcutaneously injected with 5×10^5 CT26 cells. Mice with a tumor size of up to 75 mm³ were then treated with an intraperitoneal injection of 250 µg/mouse of either isotype control (400671, Biolegend) or anti-CD20 antibody (152115, Biolegend). Two days later, the mice were intraperitoneally injected with 200 µg of isotype control (BE0089, Bioxcell) or anti-PD1 antibody (BE0146, Bioxcell) every three days. Tumor volume was measured, and the data were analyzed using analysis of variance (ANOVA).

At the end of the experiment, the tumors were harvested for immunohistochemical and immunofluorescence analyses. Tumors were measured using a caliper, and tumor volumes were calculated using the following formula: volume = length × width² × 0.5.

2.17. Human colorectal tumor organoid culture

The organoid culture procedure followed previous methods [39,40]. Fresh tumor tissue samples were cut into small pieces and washed with ice-cold PBS at least five times. The tissue was then digested using a digestion buffer (1 mg/mL type IV collagenase, 20 µg/mL hyaluronidase, and 0.1 µg/mL DNase in advanced DMEM/F12) for 1 h at 37 °C. After filtering the digested tissue through 100 µm strainers and lysing the red blood cells (RBCs), the cell pellet was collected and suspended in an organoid medium supplemented with 5 % Matrigel. The cell suspension was dispensed into 96-well low-attachment-surface culture plates. On the second day, the culture medium was supplemented with 10 µg/mL anti-CD20 or anti-PD-1 antibodies. On the seventh day, the organoids were digested for flow cytometry analysis.

For human CRC organoids, the basal culture medium was prepared as follows: Advanced DMEM/F12 was supplemented with penicillin/streptomycin/gentamicin, 1 mM HEPES, 1x GlutaMAX, 100 mg/mL primocin (ant-pm-1, InvivoGen), 1xB27 (S441J7, BasalMedia), 1 mM N-acetylcysteine (616-91-1, Sigma-Aldrich), 40 ng/mL EGF (AF-100-15, preproTECH), 20 ng/mL FGF-basic (100-18B, preproTECH), 10 µM

SB202190 (A1632, APExBIO), 10 µM Y27632 (129830-38-2, AbMolo BioScience), 0.5 µM A8301 (A3133, APExBIO), 30 ng/mL HGF (CJ72, Novoprotein), 10 nM Prostaglandin E2 (363-24-6, Tocris), 10 mM Nicotinamide (98-92-0, Sigma-Aldrich), 500 mg/mL Rspordin1 (11083-H08H, Sino Biological), and 100 ng/mL Noggin (CB89, novoprotein).

2.18. Flow cytometry

After the organoids were digested with TrypLE™ Express (12605-010, Gibco) at 37 °C for 10 min, they were washed with PBS. The cells were then stained with fluorophore-labeled antibodies in PBS, following the manufacturer’s instructions. The antibodies used for the flow cytometry are listed in *Supplementary Table 3*. The stained samples were immediately acquired, and fluorescence levels were measured using a CytoFLEX fluorescent cell analyzer (Beckman Coulter). The data obtained were analyzed using the FlowJo software.

2.19. Statistical analysis

All statistical analyses were performed using GraphPad Prism 9. A two-tailed unpaired t-test was employed to determine statistical significance when comparing the means between the two groups. When comparing multiple values to a single value, one-way ANOVA with Dunnett correction was used. For comparisons among multiple values, Tukey correction was applied. A p-value less than 0.05 was considered statistically significant.

3. Results

3.1. The immune landscape of colorectal cancer in different regions

Five samples from two patients were collected for single-cell RNA sequencing (scRNA-seq). We integrated our own scRNA-Seq data (stored at GSE221575) and an additional fourteen samples obtained from seven patients in the GSE132465 dataset [16] (*Table S1*) to decipher tumor heterogeneity and the immune microenvironment across various regions in CRC. After initial quality control and batch effect removal, 39,484 cells derived from nine patients were retained for subsequent analysis, which included nine tumor samples, nine paired adjacent normal colon samples from three different regions of the colorectum, and one corresponding liver metastasis tumor sample (*Fig. 1A*). We applied t-distributed stochastic neighbor embedding (t-SNE) to the sequencing data to identify prominent cell clusters within both colorectal normal and tumor samples (*Fig. 1B* and *S1A*). Based on the expression of canonical markers (*Fig. 1C* and *S1B*, *Table S5*), we identified six principal clusters comprising three immune cell clusters (myeloid, T, and B cells) and three non-immune cell clusters (epithelial cells, fibroblasts, and endothelial cells) (*Fig. 1B*). *Fig. S1C* displays the top 10 DEGs. Although the proportion varied, each cluster was present in all samples, with immune cell types predominating in most samples (*Fig. S1D*). We investigated the correlation between immune cell infiltration in CRC and genetic mutations, as well as tumor stages, revealing that the proportions of myeloid, T, and B cells were comparable across early and late stages and between wild-type and mutant KRAS and BRAF patients (*Figs. S2A–C*). Given that the study included only one MSI-H patient, we could not establish a reliable association between MSI status and immune infiltration. Subsequently, we hypothesized that the composition of cell types might be influenced by the tumor regions. The 19 samples were categorized into seven groups: ascending normal (AN, n = 3), ascending tumor (AT, n = 3), sigmoid normal (SN, n = 3), sigmoid tumor (ST, n = 3), rectum normal (RN, n = 3), rectum tumor (RT, n = 3), and liver metastasis (LM, n = 1) (*Fig. 1D*). Most cells in the LM sample were epithelial and myeloid, with significantly fewer T and B cells, suggesting that the metastatic tumor exhibited the lowest immunogenicity, potentially indicating complete immune escape (*Fig. 1D*) [41]. Despite the limited sample size of liver metastases, our findings

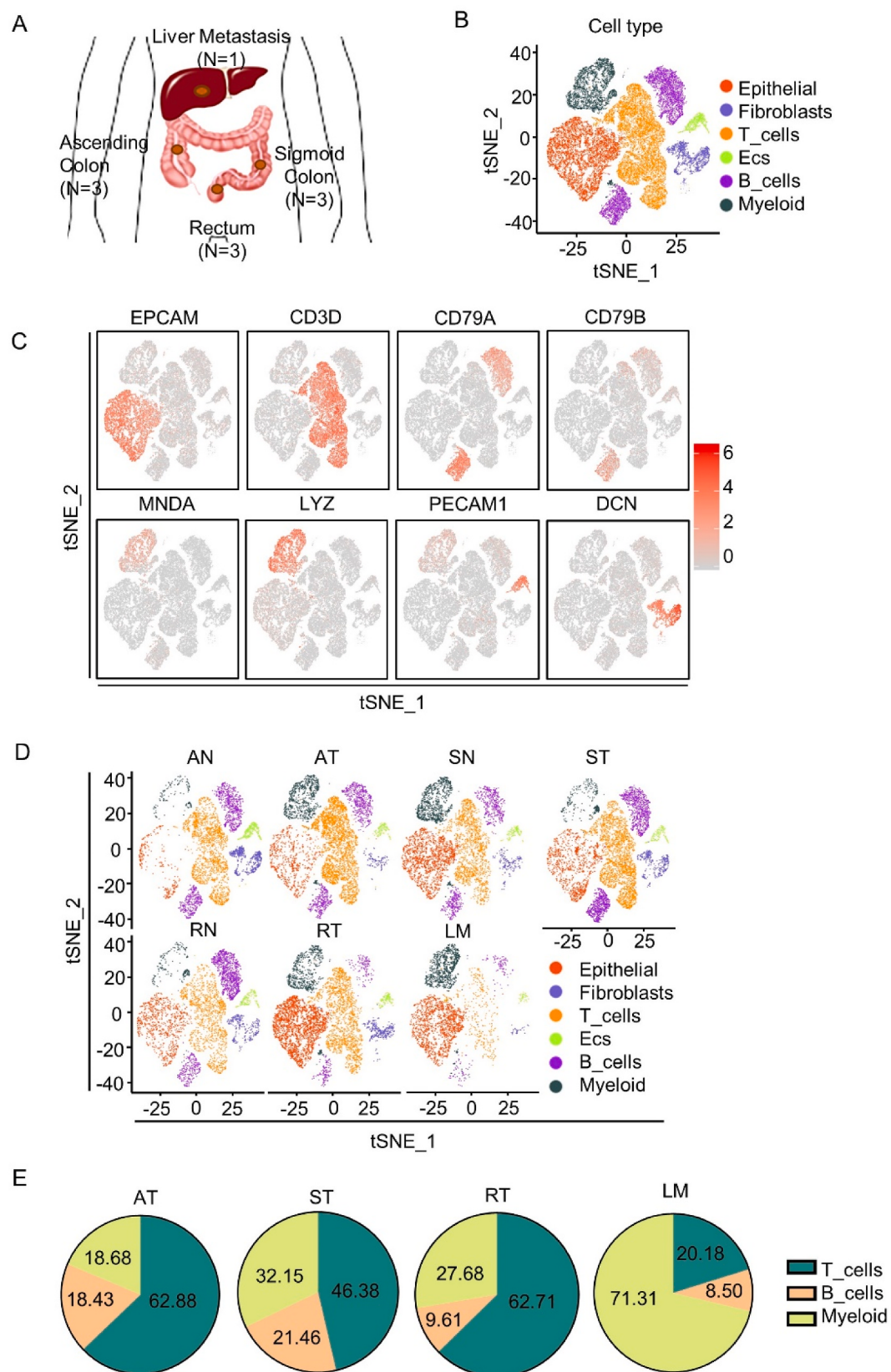


Fig. 1. The distinct immune landscape of different regions in colorectal cancer. A. Overview of the study design. Colorectal tumor, normal, and liver metastasis samples from nine patients from different regions were analyzed. B. t-distributed stochastic neighbor embedding (t-SNE) plot of the six main cell types identified in the CRC lesions. C. Feature plots present the normalized expression levels of eight representative canonical marker genes across six clusters. D. t-SNE plots of main cell clusters representing sample origin, ascending normal (AN), ascending tumor (AT), sigmoid normal (SN), sigmoid tumor (ST), rectum normal (RN), rectum tumor (RT), and liver metastasis (LM). E. Immune cell distribution of tumor tissues in different regions, including AT, ST, RT, and LM.

align with those of prior research [42]. Nonetheless, T cells in ST and RT samples demonstrated a reduced ratio compared to AT in primary CRC tumors, corroborating earlier reports that right-sided colon cancer (RCC) is characterized by greater immunogenicity and T-cell infiltration (Fig. 1E) [43]. Our analysis revealed a gradual decrease in immune infiltration from the proximal to distal end of the intestine, with T cells constituting the predominant cluster. Statistical analyses were conducted on the immune cell types to evaluate the overall pattern of immune infiltration across different regions (Fig. S2D). Myeloid cells emerged as the dominant immune cell type, with a decrease in T-cell infiltration in LM tissues (Fig. 1E). Multiple regions of CRC display distinctive TMEs, indicating variation in the tumor immune landscape from the proximal to the distal colorectum.

3.2. T cells infiltrated more in right-sided colon cancer

Subsequent re-clustering of T cells yielded six distinct clusters (Figs. S3A–C). We conducted a heatmap analysis of established functional gene sets to elucidate the functions of different T-cell subpopulations [11,44]. The $\gamma\delta$ T cells, characterized by high TRGC1 expression, additionally exhibited GZMA and NKG7 (Figs. S3D–E), in line with previous reports [23]. CD8 effector T cells, marked by elevated levels of GZMA and NKG7 expression, can be identified as cytotoxic T cells (Figs. S3D–E and 4A–B). Exhausted T cells, manifesting exhaustion markers such as HAVCR2 and LAG3, expressed cytotoxic markers, suggesting retention of T-cell activation and cytotoxic function despite the exhaustion state (Figs. S3D–E and 4A–B).

Comparison of T-cell subcluster proportions between adjacent normal and tumor samples revealed a reduction in CD8 effector T cells and an increase in Tregs and exhausted T cells within tumors, characteristic of an immunosuppressive tumor environment (Figs. S3F and 4C). Although the overall trend of major subclusters remained consistent between normal and tumor tissues, the patterns of T-cell and CD8 effector T infiltration differed notably between ascending and sigmoid tumor tissue samples. Notably, T cells, particularly CD8⁺ T and $\gamma\delta$ T cells, displayed a higher degree of infiltration in RCC within the discovery cohort (Figs. S4D–F), consistent with findings from other studies [45]. Due to the limited sample size of our initial cohort, we incorporated the GSE44076 dataset [46] as a validation cohort and conducted immuno-infiltration analysis using Timer 2.0 [37]. T-cell infiltration patterns in left- and right-sided CRC within the validation cohort agreed with our earlier observations (Figs. S4G–I). Although the results from our samples were not statistically significant, the observed trend remained consistent. Interestingly, a substantial proportion of CD8 effector T cells was detected in the liver metastasis samples (Fig. S4C). However, the numbers were limited, potentially attributable to the low overall T-cell infiltration in the liver metastasis sample. Distinct disparities between normal and tumor samples were noted, indicating an immunosuppressive tumor environment. Furthermore, the analysis of T-cell subtypes across different regions disclosed that RCC exhibits more pronounced immune infiltration.

3.3. The infiltration of M1_like and M2_like macrophages in CRC

Myeloid cells constitute a complex immune cell group comprising several subtypes that play crucial roles in tumor development [15]. Based on marker gene expression (Figs. S5D–G, Table S5), myeloid cells were categorized into three main subtypes: macrophages, dendritic cells, and mast cells (Figs. S5A–C). Based on DEGs, the macrophages were divided into three subtypes: M1_like_macro, M2_like_macro, and proli_macro (Fig. S5A). The proportional distribution demonstrated that macrophage cells constituted most myeloid cells in tumor samples, while dendritic and mast cells were more prevalent in normal tissues (Fig. S6A), underscoring the significant role of macrophages in the tumor microenvironment. Macrophages accounted for up to 90 % of myeloid cells present in the liver metastasis samples (Fig. S6A). We

observed higher levels of macrophage infiltration in the liver metastasis sample than in the normal and primary tumors for both M1_like and M2_like upon examining the degree of macrophage infiltration in the respective samples (Fig. S6C). This trend was also evident in the GSE50760 cohort [47] (Fig. S6E), which served as a validation cohort. Upon comparing macrophages in samples from different regions, the infiltration patterns of the two cell types, M1_like macro and M2_like macro, were opposed between AT and ST groups (Fig. S6B). Consequently, we investigated the potential differences in the distribution of macrophage subtypes between the left and right colon, as evidenced by the GSE44076 cohort (Fig. S6D). M1_like macro was predominant in left-sided colon cancer (LCC), whereas M2_like macro was more prevalent in RCC. The distribution trends of M1_ and M2_like macrophages in right- and left-sided CRC are consistent with the GSE44076 cohort but require further verification through an expanded sample size.

We conducted an enrichment analysis on M1_like and M2_like macrophages between AT and ST groups to investigate functional differences in macrophage populations across different sites (Figs. S6F–G). M1_like macro demonstrated functional enrichment in inflammatory-related pathways, transcriptional regulation, and B-cell receptor signaling pathways within the ST group. M2_like macro interacted with leukocytes in the AT group. The chemokine signaling pathway was associated with the upregulation of M2_like macro in the AT group and M1_like macro in the ST group, reflecting the recruitment and adhesion of B cells to myeloid cells. These results indicate that the infiltration patterns of M1_like and M2_like macrophages are opposite in RCC and LCC and that they interact with B cells in CRC.

3.4. Landscape of the heterogeneity and diversity of B cells in CRC

We performed subclustering on B cells, revealing six distinct clusters, aiming to further understand B-cell behavioral characteristics (Fig. 2A and S7A–B), including Memory B, Naive B, IgA Plasma, IgG Plasma, Proli Plasma, and germinal center B cells (GCBs), with their markers displayed in Fig. 2B and S7C, and Table S5. Tumor samples contained fewer naive B cells than the adjacent normal samples, and notably, naive B cells were absent in the ST samples (Fig. 2C and S7F–G). In both adjacent normal and tumor samples, B-cell clusters were predominantly composed of plasma cells (Fig. 2C). The infiltration of plasma cells in tumor samples was lower than in adjacent normal tissues (Fig. 2C and D). The observed differences were further validated in the GSE44076 cohort (Fig. S7D). Additionally, our findings revealed that IgA plasma cells constituted most plasma cells in normal samples, whereas IgG plasma cells were present in smaller proportions. Interestingly, this ratio was reversed in the tumor samples (Fig. 2C and D). Previous studies [48–51] have demonstrated the crucial role of chemokine receptors CCR9, CCR10, CXCR3, and CXCR4 in the migration of plasma cells. A comparison of chemokine receptor expression in plasma cells was conducted between normal and tumor tissues, revealing upregulation of CXCR3 and CXCR4 in IgG plasma cells from tumor tissues (Fig. S7E). This finding potentially provides an explanation for the observed higher frequency of IgG plasma cells in tumor samples. The percentage of plasma cells increased in the liver metastasis sample, which was further confirmed in another validation cohort, GSE50760 (Figs. S7H–I). In conclusion, the infiltration patterns of B-cell subclusters varied between normal and tumor samples, with tumor-associated plasma cells predominantly displaying an IgG phenotype.

3.5. Developmental trajectories of B cells in different regions of CRC

Pseudotime analysis was conducted to infer the maturation course and explore the evolutionary trajectory of B-cell subtypes (Fig. 2E). According to the current understanding of B-cell development, naive B cells differentiate into memory B cells and plasma cells in response to external antigen stimulation [52]. Consequently, naive B cells were selected as the initial point of the differentiation trajectory (Fig. 2E).

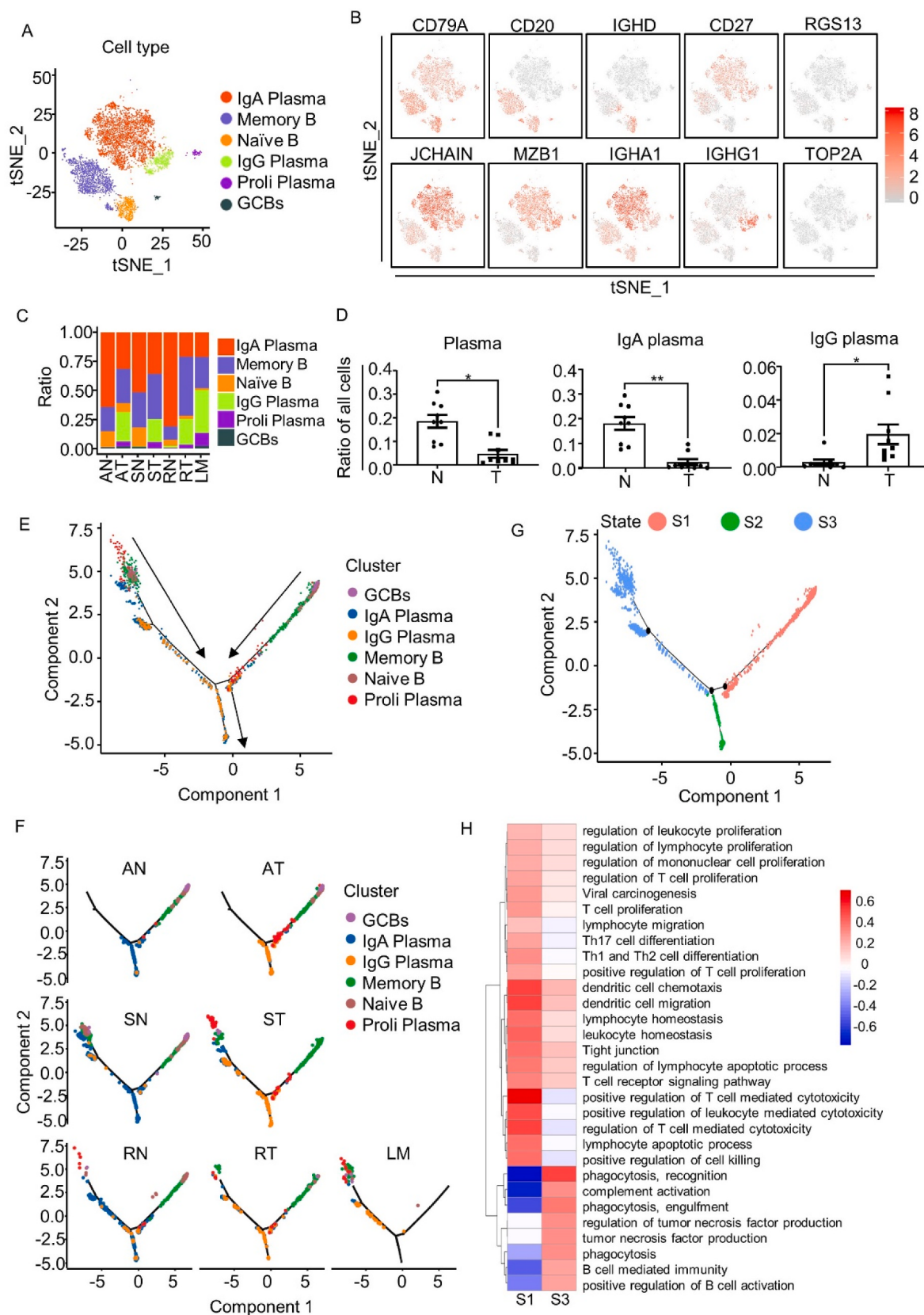


Fig. 2. Analysis of B-cell subclusters and developmental trajectory. **A.** t-SNE plot of the six main subclusters of B cells. **B.** Feature plots illustrate the normalized expression levels of ten representative canonical marker genes across six main subclusters of B cells. **C.** The proportion of each B-cell subcluster in the AN, AT, SN, ST, RN, RT, and LM samples. **D.** Comparison of the percentage of plasma cells, including IgG and IgA plasma cells in tumor and normal samples. * $p < 0.05$, ** $p < 0.01$. **E-F.** The trajectory plot illustrates the dynamics of B-cell subclusters in all samples and samples from different regions (AN, AT, SN, ST, RN, RT, and LM). **G.** Trajectory analysis of B cells annotated by the cellular state. **H.** Heatmap of the differences in pathway activities between S1 and S3.

Pseudotime analysis was stratified into distinct groups based on cell origin (Fig. 2F). Throughout development, cells have distinct gene expression programs that determine their fate, resulting in the formation of separate branches in pseudotime analysis. The trajectories of B cells were classified into three branches, each corresponding to a distinct state designated as S1, S2, and S3. A distinct developmental trajectory was observed in S1 and S3 stages (Fig. 2F and G). Differential enrichment analysis was conducted on S1 and S3 to investigate these differences (Fig. 2H). The enrichment results demonstrated the regulation of lymphocyte and monocyte proliferation, adhesion, and migration in the S1 section, which were absent in LM samples. In contrast, S3 section, excluding RCC samples, exhibited enrichment for specific innate immune functions, including enhanced B-cell activation through phagocytosis and complement activation. Comprehensive B-cell analyses provided insights into their functions during CRC occurrence and development. B cells exhibited distinct differentiation and developmental patterns in different regions of CRC. B cells had the potential to interact with other immune cells that play critical roles in CRC; accordingly, further investigation of these interactions is warranted.

3.6. B cells have extensive interactions with other immune cells, especially CD20⁺ subgroup

While exploring the development of B cells, we discovered that they interact closely with other immune cells in different regions (Fig. 2H and S6F-G). Several studies have also demonstrated that direct or indirect actions of T cells and macrophages are required for B-cell activation during carcinogenesis [53,54]. Andreu et al. demonstrated that B cells produce antibodies against extracellular matrix components at the tumor site with the aid of CD4⁺ T cells [55]. Another study indicated that B cells and antibodies play a crucial role in orchestrating macrophage-driven, tumor-promoting inflammation [56]. Consequently, we utilized CellPhoneDB [35] to investigate cell-cell communication networks within major cell clusters and assess whether regional differences in cellular composition impact cell-cell interactions. B cells primarily interacted with myeloid cells in whole specimens (Fig. 3A) or in AT, ST, RT, and LM samples (Fig. 3B), and the interaction was more pronounced in tumor tissues than in normal tissues (Fig. 3C). We deduced the specific receptor-ligand (R-L) interactions between B cells and myeloid cells in each region to further investigate how these interactions affect the tumor microenvironment (Fig. 3D). The interactions of LAMP1_FAM3C, MERTK_GAS6, HLA-C_FAM3C, and SPP1_CD44 were upregulated in several tumors, implicated in tumor development [57–61], and were increased in all tumor samples. Putative R-L interactions between B cells and myeloid cells exhibited regional heterogeneity within each region, with certain interactions being rare or unique to specific regions. SEMA4A_PLXND1, which enhances macrophage migration [62], was upregulated in ascending tumor samples. HLA-DPB1_NRG1, CD52_SIGLEC10, and LTBR_LTB were predicted to be upregulated in sigmoid and rectal tumor samples. CD52 SIGLEC10 inhibited the proliferation and activation of immune cells [63], consistent with the lower immune infiltration found in sigmoid and rectal samples than in ascending samples. As expected, certain receptor-ligand pairs linked to invasion, adhesion, and metastasis, such as ANXA1_FPR1 [64], LAIR1_LILRB4 [65], and FN1_a4b1 complex [66], demonstrated an increase in the LM sample. Despite regional differences, B cells exerted their influence on the tumor immune microenvironment through direct or indirect interactions.

We obtained a gene list of B cells compared with other cell clusters and identified a set of B-cell characteristic genes (Table S4) by selecting genes with an adjusted p-value <0.05, fold change >1, and PCT1 > PCT2 to examine a specific population of B cells, which helped determine the clinical relevance and function of B cells in tumor progression. Subsequently, survival analysis of these characteristic genes was conducted using cohort data of colon and rectal adenocarcinomas from The Cancer Genome Atlas (TCGA) (Fig. S8A). CD20⁺ B and TNFRSF17⁺ B

cells were associated with favorable overall survival in all samples (Fig. 3E and S8A). Furthermore, subsequent survival analyses were conducted on B-cell characteristic genes in RCC, LCC, and rectal cancer (RC) samples from TCGA (Fig. 3F and S8B-D) to further investigate the relationship between B-cell characteristic genes and prognosis in samples from different regions. Specifically, CD79B, CD20, TNFRSF17, and SMIM14 were associated with a favorable prognosis in RCC (Fig. 3F and S8B). UBE2J1 was associated with a favorable prognosis in LCC (Fig. S8C), and PRDX4 and SSR4 were associated with a favorable prognosis in RC (Fig. S8D). The survival curve showed that CD20 had the most significant p-value and a long-term survival benefit. Therefore, we focused on the CD20⁺ B-cell subpopulation. To confirm the potential regulation of CD20⁺ B cells in the tumor immune microenvironment, we utilized NicheNet [36] to infer cell-cell interactions using a prior model of ligand-target regulatory potential. We identified the top predicted immune receptor-ligand interactions that were differentially regulated in tumors based on gene expression in our scRNA-seq data (Figs. S9C–D). GO enrichment analysis of predicted receptors indicated that CD20⁺ B cells tended to recruit and adhere to other lymphocytes (Fig. 3G). The simultaneous presence of intratumoral CD20⁺ B cells and CD8⁺ T cells has been linked to extended survival in CRC or other cancers, irrespective of other clinical variables [18]. Additionally, Jonna et al. found a significant correlation between a higher density of CD20⁺ cells and improved OS [67]. CD20⁺ B cells might serve as prognostic indicators for colorectal tumor patients, particularly RCC, and modulate the TME through interactions with other immune cells.

3.7. CD20⁺ B cells predict the prognosis of patients with CRC

To validate the predicted prognostic role of CD20⁺ B cells in CRC, we conducted IHC staining on an additional cohort of 209 patients. The clinical characteristics are presented in Supplementary Table 2. In line with the aforementioned TCGA results (Fig. 3E–F and S9A–B), the IHC staining results consistently revealed a positive correlation between CD20⁺ B cells and improved survival in CRC patients, particularly in those with RCC (Fig. 4A–B and S11A). This association may be attributed to the presence of tertiary lymphoid structures [68]. We investigated the association between the densities of intratumoral CD20⁺ B cells and CD3⁺ T cells in CRC because the cell-cell interaction analyses predicted that CD20⁺ B cells regulate the TME via recruitment and adhesion of other immune lymphocytes (Fig. 3G). Simple linear correlation analysis revealed a positive correlation between the density of CD20⁺ B cells and CD3⁺ T cells (Fig. 4C). Additionally, we observed that CD20⁺ B cells were in close proximity to CD3⁺ T cells and often formed small clusters or tertiary lymphoid-like structures (Fig. 4E and S10A). These structures were observed within the tumor bed and at the infiltrating margin. Considering the correlation between CD20⁺ B cells and T cells, as well as their close spatial relationship, we examined their impact on patient survival when considering their respective densities. As previously reported, the presence of CD3⁺ T cells predicted survival in patients with CRC (Fig. S11B). Importantly, we found that CRC patients with high intratumoral densities of both CD20 and CD3 subsets exhibited prolonged survival compared to those with low densities of both subsets, a finding that was particularly significant in patients with RCC (Fig. 4D and S12A–B). IHC staining results confirmed a positive correlation between the densities of tumor-infiltrating B cells and improved survival in patients with CRC, with the strongest association observed in patients with RCC. These findings suggested a synergistic effect between B cells and T cells, particularly in the context of RCC.

3.8. The depletion of CD20⁺ B cells inhibits tumor killing in vivo and in vitro

Next, we conducted validation experiments to further support the crucial role of CD20⁺ B cells in CRC. We utilized CT26 murine models, where Balb/c mice were subcutaneously transplanted with 5×10^6

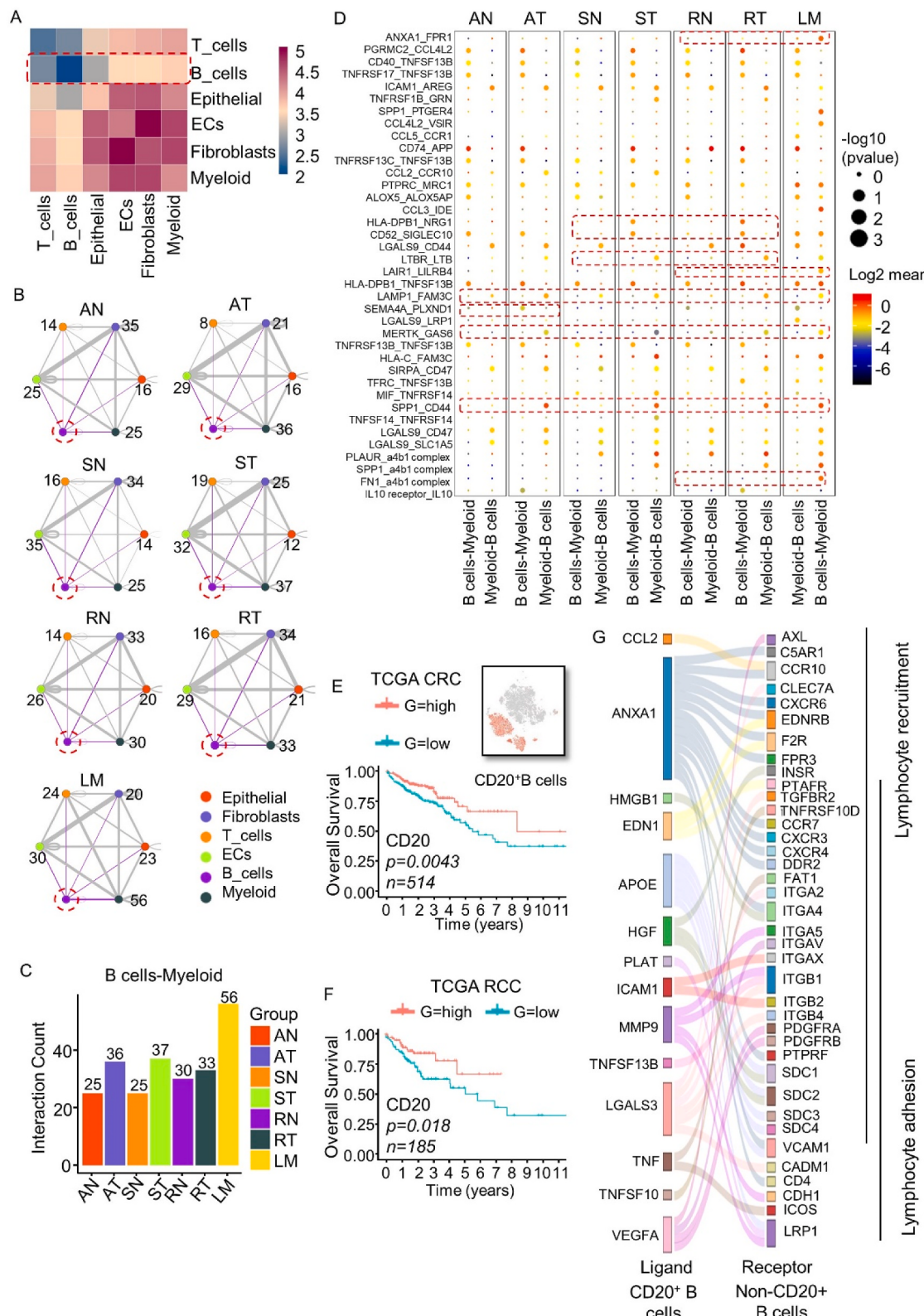


Fig. 3. B cells have extensive interaction with other immune cells, especially $CD20^+$ subgroup. A. Heatmap displaying the key cell-cell interaction pairs in the samples. B. Circos diagram in different regions presents cell-cell communication between B cells and other main clusters. The size of the line represents the total number of ligand-receptor pairs. C. Column bar chart of the total number of ligand-receptor pairs between B cells and myeloid cells in different regions. D. Overview of selected ligand-receptor interactions between B cells and myeloid cells. E-F. Kaplan-Meier overall survival curves of CD20 in TCGA CRC (E) and right-sided colon cancer (RCC) (F). G. Sankey diagram indicating selected ligand-receptor pairs significantly over-represented in CRC as determined by NicheNet between $CD20^+$ B cells (ligands) and other immune cells (receptors).

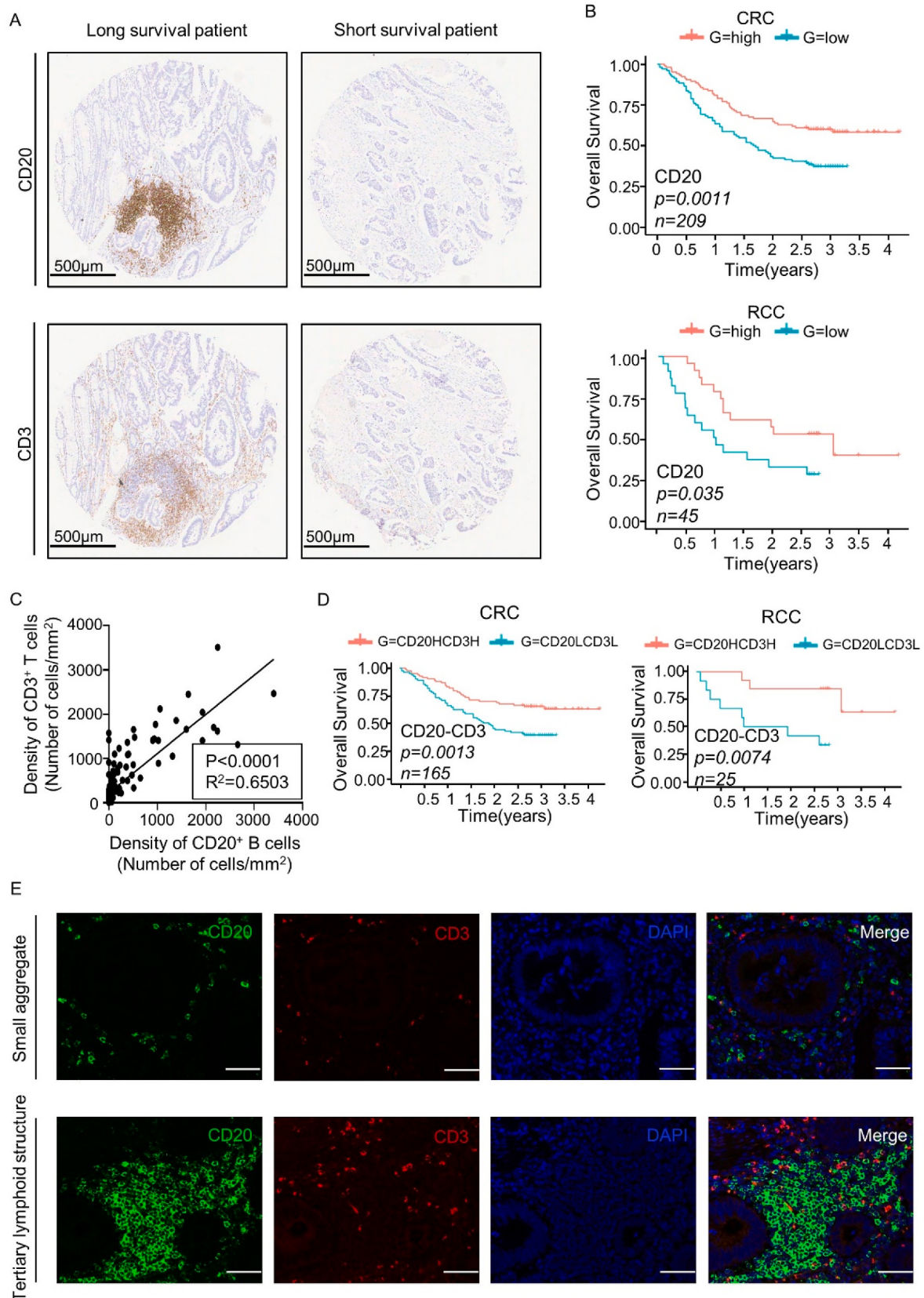


Fig. 4. CD20⁺ B cells predict the prognosis of CRC patients. A. Representative IHC images of CD20 and CD3 from long- and short-survival patients. Bar = 500 µm. B. Kaplan-Meier (KM) curves of CD20⁺ B cells in CRC and RCC patients. C. The density of CD20⁺ B cells was associated with CD3⁺ T cells. D. Kaplan-Meier (KM) curves of CD20^HCD3^H versus CD20^LCD3^L patients in CRC and RCC patients. The p-values were based on log-rank tests. E. Representative IF images of CD20 (green), CD3 (red), and nuclear staining with DAPI (blue) in CRC. 200 × magnification. Bar = 50 µm.

CT26 cells and treated with reagents once the tumor volumes reached 75 mm^3 (Fig. 5A). The mice were divided into four treatment groups: control, anti-CD20, anti-PD-1, and anti-CD20+anti-PD-1, to investigate the impact of CD20⁺ B-cell depletion on tumor growth with or without

PD-1 antibody. Tumor volumes were significantly different between the treatment groups (Fig. 5B–D). Consistent with previous reports [69], we observed that anti-PD-1 treatment effectively inhibited tumor progression in CT26 models. However, depleting CD20⁺ B cells reversed this

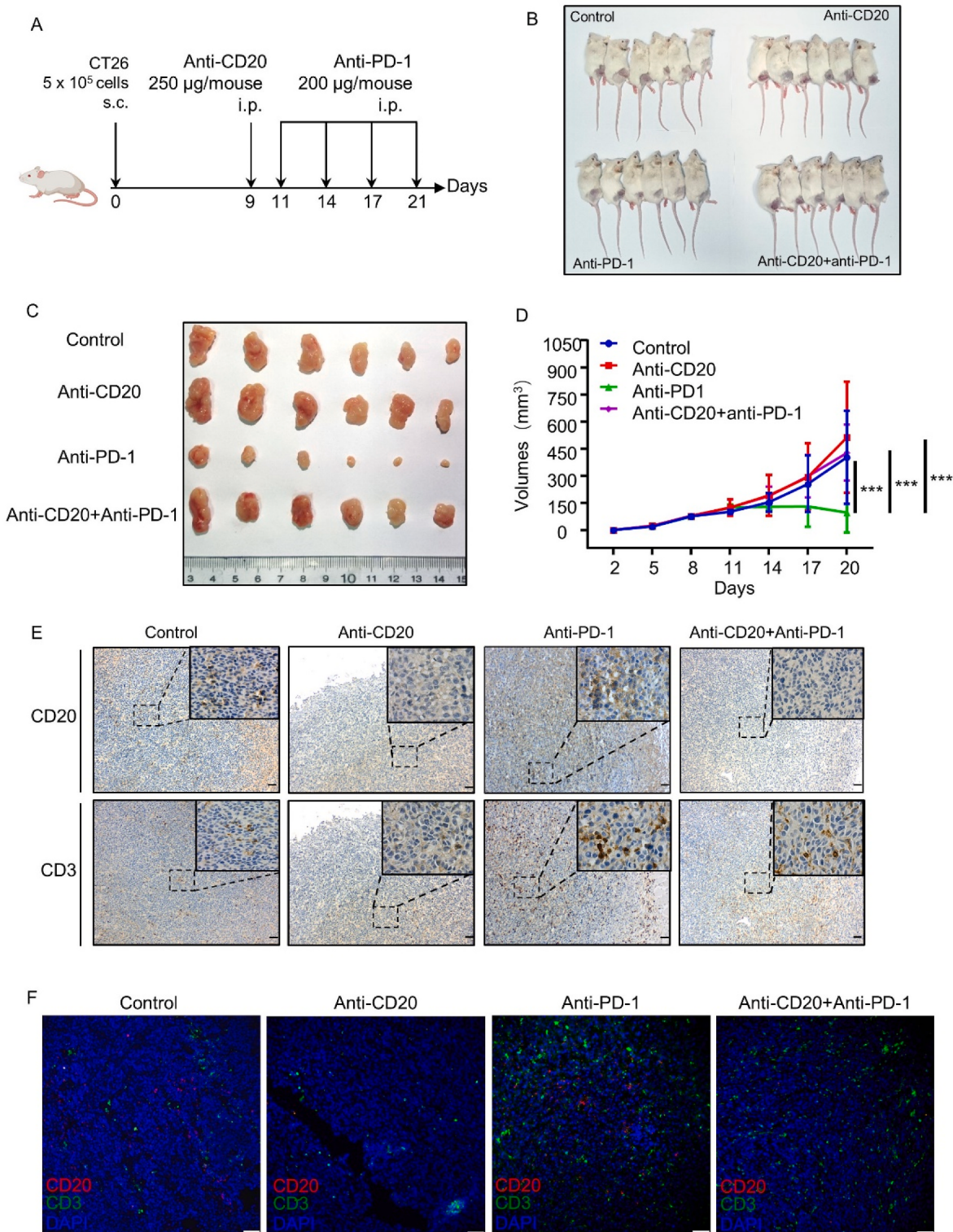


Fig. 5. Anti-CD20 reverses the inhibition of PD-1 antibody in a CRC mouse model. A. Schematic representation of the murine experimental setup. B. CT26-incubated mice in four groups: control, anti-CD20, anti-PD-1, and anti-CD20+anti-PD-1. C. Tumor samples were collected from each group. D. Tumor growth curves of CT26-injected mice in different groups. *** $p < 0.001$. E. Representative IHC images of CD20 and CD3 staining of CT26 tumor sample paraffin sections from each treatment group. Bar = 100 μm . F. Representative IF images of CD20 (red), CD3 (green), and nuclear staining with DAPI (blue) of CT26 tumor sample frozen sections from each treatment group. Bar = 100 μm .

inhibition (Fig. 5D), despite individual anti-CD20 treatment resulting in a slight promotion of tumor growth, which was not statistically significant. This suggests that CD20⁺ B cells may collaborate with T cells to resist tumor progression. To verify this hypothesis, we compared immune cell infiltration in murine tumors among different groups.

However, individual treatment with anti-CD20 resulted in decreased T-cell infiltration (Fig. 5E and F).

To further support the anti-tumor role of CD20⁺ B cells in CRC, we generated patient-derived organoids from surgical resections of CRC (Fig. 6A). Tumor and immune cells obtained from CRC samples were

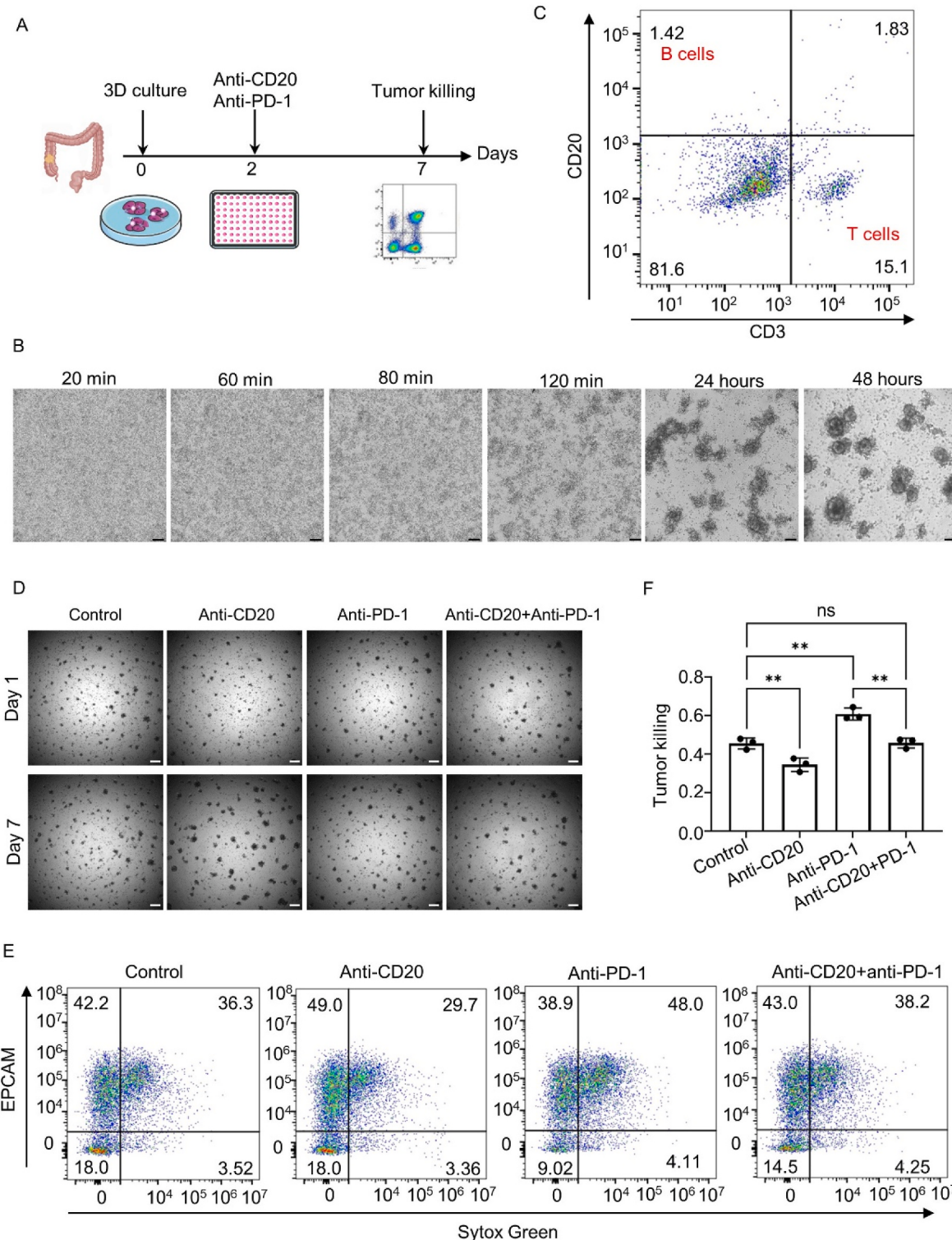


Fig. 6. The depletion of CD20⁺ B cells reduces tumor killing in the patient-derived organoid model. A. Overview of the timeline of patient-derived organoid generation and experimental treatment. B. Time course of primary cell migration and self-assembly in the first 120 min, 24 h, and 48 h. C. Flow cytometry plots gated on CD3⁺ T and CD20⁺ B cells of patient-derived organoids. D. Representative bright-field images of patient-derived organoids on day seven in the different experimental groups. Bar = 100 μ m. E, Representative flow cytometry plots gated on Epcam⁺ cells and Sytox Green tested for reactivity against different experiments after five days of treatment. ** p < 0.01.

cultured in a low-attachment-surface dish, allowing these primary cells to form clusters through migration and self-assembly (Fig. 6B). Flow cytometry assays confirmed the presence of CD3⁺ T cells and CD20⁺ B cells in the patient-derived organoid models (Fig. 6C). Similar to the murine experiment, patient-derived organoids were divided into four groups. The addition of anti-CD20 diminished the tumor-killing effect of anti-PD-1 treatment, as demonstrated by flow cytometry assays (Fig. 6D–F). The results of our *in vivo* and *in vitro* experiments indicate that CD20⁺ B cells are crucial for tumor growth and may improve the tumor-killing effects of anti-PD-1 treatment.

4. Discussion

Here, we constructed a CRC cell atlas and characterized the immune features of CRC at various locations. We discovered varying patterns of immune cell infiltration in the TME. T cells constitute the primary immune component in primary tumor samples, whereas myeloid cells predominate in the liver metastasis sample, a finding consistent with the ‘immune desert’ phenomenon observed in metastases [41]. GUO et al. [17] investigated the differences in cancer cells, T cells, and macrophages between left- and right-sided colon cancer. Furthermore, B-cell infiltration progressively diminished from the proximal to the distal end of the intestine. Consequently, we concentrated our investigation on the role of B cells in CRC at various locations.

B cells are categorized into two distinct groups: mature B cells and plasma cells. We noted a phenotypic switch in plasma cells between normal and tumor samples. The proportion of IgA plasma cells declines, whereas that of IgG plasma cells increases in tumor cells. This shift may be attributed to the impaired migration of IgA-secreting cells, which could induce further inflammatory responses and promote tumor growth in the colon [70]. Unlike WANG et al. [23], who analyzed the differences between multi-loci samples from the same tumor, we concentrated on the disparities between tumors from various locations. Upon further analysis of B-cell differentiation trajectory, we discovered that B cells from right- and left-sided CRC exhibit similar and divergent developmental pathways. Gene enrichment analysis of the shared differentiation trajectory revealed B-cell regulation of lymphocyte and monocyte proliferation, adhesion, and migration. Further cell interaction analyses demonstrated extensive interactions between B cells and other cell types, particularly myeloid and T cells. Further exploration of B-cell subpopulations implicated in this process suggests a potential correlation between CD20⁺ B cells and CRC progression.

We collected patient tissue samples, established a CT26 mouse model, and developed a patient-derived organoid model to elucidate the role of CD20⁺ B cells. We confirmed the association between CD20⁺ B cells and patient prognosis in CRC, particularly in RCC, through IHC staining for CD20. Furthermore, we found a correlation between CD20 expression and CD3, with a high density of CD20 coupled with high CD3 infiltration serving as a stronger predictor of prognosis in patients with CRC. Additionally, to investigate the impact of CD20⁺ B cells on CRC, we depleted these cells both *in vivo* and *in vitro*. Our findings suggest that anti-CD20 treatment may facilitate tumor progression and negate the tumoricidal effects of anti-PD-1 therapy. Investigating the correlation between CD20⁺ B cells and CRC patient prognosis, as well as the role of these cells in counteracting anti-PD-1 therapy, is of significant interest. Future studies should include larger cohorts to validate these findings. Moreover, CD20⁺ B cells comprise naive B cells, memory B cells, and GCBs. Further research is necessary to determine the relative importance of each subgroup. While depletion studies help validate the role of CD20, further investigation involving CD20 agonists is essential to directly ascertain their impact on CRC.

In summary, we delineated the unique characteristics of the immune landscape in CRC across various regions and demonstrated that the infiltration of CD20⁺ B cells correlates with both the prognosis of CRC and the therapeutic efficacy of PD-1 antibodies. These findings suggest a potential therapeutic target for clinical intervention.

Ethics approval and consent to participate

Human CRC specimens and patient clinical data were obtained from the Jinling Hospital, with the approval of the Jinling Hospital Research Ethics Committee. All mouse experiments were approved by the Institutional Animal Care and Use Committee of the Jinling hospital and performed in accordance with the Declaration of Helsinki.

Consent for publication

All authors give consent for the publication of the manuscript in *Cancer Letters*.

Data availability

All data needed to evaluate the conclusions in the paper are presented in the main text or the supplementary materials. The data generated in this study are publicly available in Gene Expression Omnibus (GEO) at GSE221575 and GSE221575.

Funding information

This work was supported by the National Natural Science Foundation of China [82072725, 81872042, 81702442, 81972332, 82002583, 82002591], the Key Program of Jiangsu Provincial Health Commission [ZD2021039], the Natural Science Foundation of Jiangsu province [BK20170623, BK20200273], the China Postdoctoral Science Foundation [2020M670090ZX, 2021MD703958], the Postdoctoral Science Found of Jiangsu province [2018K090B].

CRedit authorship contribution statement

Linlin Ji: Writing – original draft, Formal analysis, Data curation. **Gongbo Fu:** Writing – review & editing, Funding acquisition, Conceptualization. **Mengxi Huang:** Writing – original draft, Formal analysis, Data curation. **Xiaoming Kao:** Writing – original draft, Formal analysis, Data curation. **Jialong Zhu:** Writing – original draft, Formal analysis, Data curation. **Zhe Dai:** Methodology, Investigation. **Yitian Chen:** Methodology, Investigation. **Huiyu Li:** Methodology, Investigation. **Jie Zhou:** Resources, Project administration. **Xiaoyuan Chu:** Writing – review & editing, Funding acquisition, Conceptualization. **Zengjie Lei:** Writing – review & editing, Funding acquisition, Conceptualization.

Declaration of competing interest

The authors declare that they have no competing interests.

Acknowledgements

We would like to thank Singleron and Berry Oncology for technical assistance. In parts, this study relied on publicly available datasets, and we thank the authors for accessibly sharing their data.

Appendix A. Supplementary data

Supplementary data to this article can be found online at <https://doi.org/10.1016/j.canlet.2024.216664>.

References

- [1] H. Sung, J. Ferlay, R.L. Siegel, et al., Global cancer Statistics 2020: GLOBOCAN estimates of incidence and mortality worldwide for 36 cancers in 185 countries, *CA Cancer J. Clin.* 71 (2021) 209–249.
- [2] E. Dekker, P.J. Tanis, J.L.A. Vleugels, et al., Colorectal cancer, *Lancet* 394 (2019) 1467–1480.
- [3] T. Andre, K.K. Shiu, T.W. Kim, et al., Pembrolizumab in microsatellite-instability-high advanced colorectal cancer, *N. Engl. J. Med.* 383 (2020) 2207–2218.

- [4] S.Y. Yang, M.S. Cho, N.K. Kim, Difference between right-sided and left-sided colorectal cancers: from embryology to molecular subtype, *Expert Rev. Anticancer Ther.* 18 (2018) 351–358.
- [5] J.M. Loree, A.A.L. Pereira, M. Lam, et al., Classifying colorectal cancer by tumor location rather than sidedness highlights a continuum in mutation profiles and consensus molecular subtypes, *Clin. Cancer Res.* 24 (2018) 1062–1072.
- [6] M.S. Lee, D.G. Menter, S. Kopetz, Right versus left colon cancer biology: integrating the consensus molecular subtypes, *J. Natl. Compr. Cancer Netw.* 15 (2017) 411–419.
- [7] R. Dienstmann, Tumor side as model of integrative molecular classification of colorectal cancer, *Clin. Cancer Res.* 24 (2018) 989–990.
- [8] E. Hedlund, Q. Deng, Single-cell RNA sequencing: technical advancements and biological applications, *Mol. Aspect. Med.* 59 (2018) 36–46.
- [9] M. Hong, S. Tao, L. Zhang, et al., RNA sequencing: new technologies and applications in cancer research, *J. Hematol. Oncol.* 13 (2020) 166.
- [10] Y. Xiao, D. Yu, Tumor microenvironment as a therapeutic target in cancer, *Pharmacol. Ther.* 221 (2021) 107753.
- [11] Y. Mei, W. Xiao, H. Hu, et al., Single-cell analyses reveal suppressive tumor microenvironment of human colorectal cancer, *Clin. Transl. Med.* 11 (2021) e422.
- [12] Y. Liu, Q. Zhang, B. Xing, et al., Immune phenotypic linkage between colorectal cancer and liver metastasis, *Cancer Cell* 40 (2022) 424–437.
- [13] D.I. Gabrilovich, Myeloid-derived suppressor cells, *Cancer Immunol. Res.* 5 (2017) 3–8.
- [14] J. Lan, L. Sun, F. Xu, et al., M2 macrophage-derived exosomes promote cell migration and invasion in colon cancer, *Cancer Res.* 79 (2019) 146–158.
- [15] L. Zhang, Z. Li, K.M. Skrzypczynska, et al., Single-cell analyses inform mechanisms of myeloid-targeted therapies in colon cancer, *Cell* 181 (2020) 442–459.
- [16] H.O. Lee, Y. Hong, H.E. Etilioglu, et al., Lineage-dependent gene expression programs influence the immune landscape of colorectal cancer, *Nat. Genet.* 52 (2020) 594–603.
- [17] W. Guo, C. Zhang, X. Wang, et al., Resolving the difference between left-sided and right-sided colorectal cancer by single-cell sequencing, *JCI Insight* 7 (2022).
- [18] R. Cabrita, M. Lauss, A. Sanna, et al., Tertiary lymphoid structures improve immunotherapy and survival in melanoma, *Nature* 577 (2020) 561–565.
- [19] B.A. Helmink, S.M. Reddy, J. Gao, et al., B cells and tertiary lymphoid structures promote immunotherapy response, *Nature* 577 (2020) 549–555.
- [20] F. Petitprez, A. de Reynies, E.Z. Keung, et al., B cells are associated with survival and immunotherapy response in sarcoma, *Nature* 577 (2020) 556–560.
- [21] J. Chen, Y. Tan, F. Sun, et al., Single-cell transcriptome and antigen-immunoglobulin analysis reveals the diversity of B cells in non-small cell lung cancer, *Genome Biol.* 21 (2020) 152.
- [22] Q. Wang, K. Sun, R. Liu, et al., Single-cell transcriptome sequencing of B-cell heterogeneity and tertiary lymphoid structure predicts breast cancer prognosis and neoadjuvant therapy efficacy, *Clin. Transl. Med.* 13 (2023) e1346.
- [23] W. Wang, Y. Zhong, Z. Zhuang, et al., Multiregion single-cell sequencing reveals the transcriptional landscape of the immune microenvironment of colorectal cancer, *Clin. Transl. Med.* 11 (2021) e253.
- [24] B. Dura, J.Y. Choi, K. Zhang, et al., scFTD-seq: freeze-thaw lysis based, portable approach toward highly distributed single-cell 3' mRNA profiling, *Nucleic Acids Res.* 47 (2019) e16.
- [25] A. Kechin, U. Boyarskikh, A. Kel, et al., cutPrimers: a new tool for accurate cutting of primers from reads of targeted next generation sequencing, *J. Comput. Biol.* 24 (2017) 1138–1143.
- [26] A. Dobin, C.A. Davis, F. Schlesinger, et al., STAR: ultrafast universal RNA-seq aligner, *Bioinformatics* 29 (2013) 15–21.
- [27] Y. Liao, G.K. Smyth, W. Shi, featureCounts: an efficient general purpose program for assigning sequence reads to genomic features, *Bioinformatics* 30 (2014) 923–930.
- [28] S. Yang, S.E. Corbett, Y. Koga, et al., Decontamination of ambient RNA in single-cell RNA-seq with DecontX, *Genome Biol.* 21 (2020) 57.
- [29] R. Satija, J.A. Farrell, D. Gennert, et al., Spatial reconstruction of single-cell gene expression data, *Nat. Biotechnol.* 33 (2015) 495–502.
- [30] I. Korsunsky, N. Millard, J. Fan, et al., Fast, sensitive and accurate integration of single-cell data with Harmony, *Nat. Methods* 16 (2019) 1289–1296.
- [31] G. Yu, L.G. Wang, Y. Han, et al., clusterProfiler: an R package for comparing biological themes among gene clusters, *OMICS* 16 (2012) 284–287.
- [32] S. Hanzelmann, R. Castelo, J. Guinney, GSVA: gene set variation analysis for microarray and RNA-seq data, *BMC Bioinf.* 14 (2013) 7.
- [33] X. Qiu, A. Hill, J. Packer, et al., Single-cell mRNA quantification and differential analysis with Census, *Nat. Methods* 14 (2017) 309–315.
- [34] G.S. Gulati, S.S. Sikandar, D.J. Wesche, et al., Single-cell transcriptional diversity is a hallmark of developmental potential, *Science* 367 (2020) 405–411.
- [35] M. Efremova, M. Vento-Tormo, S.A. Teichmann, et al., CellPhoneDB: inferring cell-cell communication from combined expression of multi-subunit ligand-receptor complexes, *Nat. Protoc.* 15 (2020) 1484–1506.
- [36] R. Browaeys, W. Saelens, Y. Saeyns, NicheNet: modeling intercellular communication by linking ligands to target genes, *Nat. Methods* 17 (2020) 159–162.
- [37] T. Li, J. Fu, Z. Zeng, et al., TIMER2.0 for analysis of tumor-infiltrating immune cells, *Nucleic Acids Res.* 48 (2020) W509–W514.
- [38] M.I. Love, W. Huber, S. Anders, Moderated estimation of fold change and dispersion for RNA-seq data with DESeq2, *Genome Biol.* 15 (2014) 550.
- [39] S. Yin, R. Xi, A. Wu, et al., Patient-derived tumor-like cell clusters for drug testing in cancer therapy, *Sci. Transl. Med.* 12 (2020).
- [40] J.T. Neal, X. Li, J. Zhu, et al., Organoid modeling of the tumor immune microenvironment, *Cell* 175 (2018) 1972–1988.
- [41] J. Yu, M.D. Green, S. Li, et al., Liver metastasis restrains immunotherapy efficacy via macrophage-mediated T cell elimination, *Nat. Med.* 27 (2021) 152–164.
- [42] Y. Xu, Z. Wei, M. Feng, et al., Tumor-infiltrated activated B cells suppress liver metastasis of colorectal cancers, *Cell Rep.* 40 (2022) 111295.
- [43] B. Baran, N.M. Ozupak, N.Y. Tetik, et al., Difference between left-sided and right-sided colorectal cancer: a focused review of literature, *Gastroenterol. Res.* 11 (2018) 264–273.
- [44] A. Sathe, S.M. Grimes, B.T. Lau, et al., Single-cell genomic characterization reveals the cellular reprogramming of the gastric tumor microenvironment, *Clin. Cancer Res.* 26 (2020) 2640–2653.
- [45] J. Guinney, R. Dienstmann, X. Wang, et al., The consensus molecular subtypes of colorectal cancer, *Nat. Med.* 21 (2015) 1350–1356.
- [46] X. Sole, M. Crous-Bou, D. Cordero, et al., Discovery and validation of new potential biomarkers for early detection of colon cancer, *PLoS One* 9 (2014) e106748.
- [47] S.-K. Kim, S.-Y. Kim, J.-H. Kim, et al., A nineteen gene-based risk score classifier predicts prognosis of colorectal cancer patients, *Mol. Oncol.* 8 (2014) 1653–1666.
- [48] J.G. Cyster, Homing of antibody secreting cells, *Immunol. Rev.* 194 (2003) 48–60.
- [49] S. Hosomi, N. Oshitani, N. Kamata, et al., Increased numbers of immature plasma cells in peripheral blood specifically overexpress chemokine receptor CXCR3 and CXCR4 in patients with ulcerative colitis, *Clin. Exp. Immunol.* 163 (2011) 215–224.
- [50] R.V. Muthuswamy, P. Sundström, L. Börjesson, et al., Impaired migration of IgA-secreting cells to colon adenocarcinomas, *Cancer Immunology, Immunotherapy* 62 (2013) 989–997.
- [51] K. Matsuo, D. Nagakubo, S. Yamamoto, et al., CCL28-Deficient mice have reduced IgA antibody-secreting cells and an altered microbiota in the colon, *J. Immunol.* 200 (2018) 800–809.
- [52] J. Qian, S. Olbrecht, B. Boeckx, et al., A pan-cancer blueprint of the heterogeneous tumor microenvironment revealed by single-cell profiling, *Cell Res.* 30 (2020) 745–762.
- [53] W.H. Fridman, F. Petitprez, M. Meylan, et al., B cells and cancer: to B or not to B? *J. Exp. Med.* 218 (2021).
- [54] A. Mantovani, B cells and macrophages in cancer: yin and yang, *Nat. Med.* 17 (2011) 285–286.
- [55] P. Andreu, M. Johansson, N.I. Affara, et al., FcRgamma activation regulates inflammation-associated squamous carcinogenesis, *Cancer Cell* 17 (2010) 121–134.
- [56] S.C. Wong, A.L. Puaux, M. Chittezhath, et al., Macrophage polarization to a unique phenotype driven by B cells, *Eur. J. Immunol.* 40 (2010) 2296–2307.
- [57] X. Liu, Z. Luo, X. Ren, et al., The crosstalk between malignant cells and tumor-promoting immune cells relevant to immunotherapy in pancreatic ductal adenocarcinoma, *Front. Cell Dev. Biol.* 9 (2021) 821232.
- [58] S.V. Novitskiy, R. Zaynagetdinov, G. Vasilevko, et al., Gas6/MerTK signaling is negatively regulated by NF-kappaB and supports lung carcinogenesis, *Oncotarget* 10 (2019) 7031–7042.
- [59] S. Loges, T. Schmidt, M. Tjwa, et al., Malignant cells fuel tumor growth by educating infiltrating leukocytes to produce the mitogen Gas6, *Blood* 115 (2010) 2264–2273.
- [60] G.H. Rao, H.Y. Wang, B.W. Li, et al., Reciprocal interactions between tumor-associated macrophages and CD44-positive cancer cells via osteopontin/CD44 promote tumorigenicity in colorectal cancer, *Clin. Cancer Res.* 19 (2013) 785–797.
- [61] S. Yin, F.F. Chen, P. Ye, et al., Overexpression of FAM3C protein as a novel biomarker for epithelial-mesenchymal transition and poor outcome in gastric cancer, *Int. J. Clin. Exp. Pathol.* 11 (2018) 4247–4256.
- [62] C. Meda, F. Molla, M. De Pizzol, et al., Semaphorin 4A exerts a proangiogenic effect by enhancing vascular endothelial growth factor-A expression in macrophages, *J. Immunol.* 188 (2012) 4081–4092.
- [63] E. Bandala-Sánchez, Y. Zhang, S. Reinwald, et al., T cell regulation mediated by interaction of soluble CD52 with the inhibitory receptor Siglec-10, *Nat. Immunol.* 14 (2013) 741–748.
- [64] L. Vecchi, M. Alves Pereira Zoia, T. Goss Santos, et al., Inhibition of the AnxA1/FPR1 autocrine axis reduces MDA-MB-231 breast cancer cell growth and aggressiveness in vitro and in vivo, *Biochim. Biophys. Acta Mol. Cell Res.* 1865 (2018) 1368–1382.
- [65] Z. Li, M. Deng, F. Huang, et al., LILRB4 ITIMs mediate the T cell suppression and infiltration of acute myeloid leukemia cells, *Cell. Mol. Immunol.* 17 (2020) 272–282.
- [66] H. Wu, R. Zhu, B. Zheng, et al., Single-cell sequencing reveals an intrinsic heterogeneity of the preovulatory follicular microenvironment, *Biomolecules* 12 (2022).
- [67] J. Berntsson, B. Nodin, J. Eberhard, et al., Prognostic impact of tumour-infiltrating B cells and plasma cells in colorectal cancer, *Int. J. Cancer* 139 (2016) 1129–1139.
- [68] Y. Mao, X. Wang, L. Xi, et al., Prediction values of tertiary lymphoid structures in the prognosis of patients with left- and right-sided colon cancer: a multicenter propensity score-matched study, *Int. J. Surg.* 109 (2023) 2344–2358.
- [69] W.W. Ho, I.L. Gomes-Santos, S. Aoki, et al., Dendritic cell paucity in mismatch repair-deficient colorectal cancer liver metastases limits immune checkpoint blockade efficacy, *Proc. Natl. Acad. Sci. U. S. A.* 118 (2021).
- [70] R.V. Muthuswamy, P. Sundstrom, L. Börjesson, et al., Impaired migration of IgA-secreting cells to colon adenocarcinomas, *Cancer Immunol. Immunother.* 62 (2013) 989–997.